

## Article

# Optimization of Supply Air Parameters Control Based on Gappy POD Method for Creating Non-Uniform Temperature Fields

Xin Wang, Yuhong Liu, Zhiyin Cao, Dekang Li, Jinchi Zhao and Wenbing Weng \*

School of Environment and Architecture, University of Shanghai for Science and Technology, 516 Jungong Road, Yangpu District, Shanghai 200093, China; wangxinshiyun@126.com (X.W.); liuyuhong825@163.com (Y.L.); caozhiyinbetter@163.com (Z.C.); 212272050@st.usst.edu.cn (D.L.); zhaojinchi2022@163.com (J.Z.)

\* Correspondence: wenbing@vip.163.com; Tel.: +86-139-0173-6714

**Abstract:** This paper explores the implementation and application of non-uniform ambient fields from two perspectives: constant heat source and abrupt heat source variation. On the one hand, the proper orthogonal decomposition (POD) method is used to find the optimum air supply parameters for different target temperatures at multiple demand points. The one-parameter, two-parameter and three-parameter cases were considered, respectively, and the parameters obtained from the search for optimisation were verified, yielding mean deviations of 0.405 K, 0.368 K and 0.380 K and mean errors of 1.48%, 1.61% and 1.68%, respectively. The accuracy of the reconstructed results of the POD method and the reliability of the POD method for finding the best results are verified step by step with the help of the experimental platform. The validation results show that the average error between the reconstructed data and the experimental data for the POD method does not exceed 5%; the average errors between the measured and set demand temperatures at the target point are 1.2% and 0.8%. On the other hand, the gappy POD method is used to accurately fill in the elements of the system with arbitrary missing data and to reconstruct the flow field in the presence of missing (gappy) data with a limited number of sensors combined with POD. The errors of the gappy POD method reconstruction are 0.54% and 1.75%. POD and gappy POD methods can better create non-uniform temperature fields in practical scenarios according to actual needs. The results of the study can provide a methodological reference for real-time reconstruction and real-time control of the indoor flow field environment. It also serves as a help and suggestion for the actual project in terms of end-regulation system and reverse design method.

**Keywords:** proper orthogonal decomposition; non-uniform environment; reconfiguring fluidity; reverse design



**Citation:** Wang, X.; Liu, Y.; Cao, Z.; Li, D.; Zhao, J.; Weng, W. Optimization of Supply Air Parameters Control Based on Gappy POD Method for Creating Non-Uniform Temperature Fields. *Buildings* **2023**, *13*, 1690. <https://doi.org/10.3390/buildings13071690>

Academic Editor: Antonio Caggiano

Received: 25 May 2023

Revised: 21 June 2023

Accepted: 28 June 2023

Published: 30 June 2023



**Copyright:** © 2023 by the authors. Licensee MDPI, Basel, Switzerland. This article is an open access article distributed under the terms and conditions of the Creative Commons Attribution (CC BY) license (<https://creativecommons.org/licenses/by/4.0/>).

## 1. Introduction

With the increasing awareness of energy saving, the establishment of a synergistic control mechanism between local and overall different demand points, ventilation and air conditioning, and the exploration of the balance between non-uniform heat load and air conditioning supply cooling/heating has become an important issue discussed by researchers. The traditional approach to design methods for creating a non-uniform environment by varying the air supply parameters is currently the trial-and-error method [1], where the design parameters are continuously adjusted to obtain the desired environmental field. Zhao et al. [2] used computational fluid dynamics (CFD) simulations to analyse the effect of different air outlet locations on indoor percentage of dissatisfied (PD), vertical temperature difference and ventilation efficiency in displacement and hybrid ventilation modes to obtain the optimum air outlet location. Tian et al. [3] calculated the flow, temperature and air age fields by solving the Navier–Stokes system of equations several times and determined the predicted mean vote (PMV), PD and air age of the office when the supply

air temperature is increased from 19 °C to 21 °C, thus finding the design parameter interval of the ventilation system to meet the indoor thermal comfort and air quality requirements. The above trial-and-error approach requires the calculation and evaluation of the artificial environment for all operating conditions and then the selection of the relatively best solution from these, which takes much calculation time and may still not lead to the best design solution. By contrast, the inverse design approach [4–7] allows the heat source intensity to be back-calculated directly from the target and obtains the environmental design parameters, which has greater potential for creating non-uniform environmental fields. Zhao et al. [8] adjusted the parameters based on the adaptive step-by-step accompanying method of CFD to complete the inverse calculation of the optimal air supply parameters for indoor environments. Zhang and You [9] used an artificial neural network (ANN) instead of CFD and combined it with a genetic algorithm for the design of the cabin environment, reducing the computational cost by 97%.

However, the inverse design method requires fast and accurate flow field information as a basis. Therefore, to improve the speed of response to the simulation of the flow field distribution, the flow field needs to be reconstructed in real time. Currently, three main approaches are used for constructing indoor flow field environments: in-space data interpolation, computational fluid dynamics and data-driven methods. In general, kriging is the most widely used spatial interpolation method [10], facilitating the effective estimation of indoor heat maps [11] and pollutant distributions [11–13] based on sensor measurements. However, the accuracy of the actual flow field interpolation largely depends on the location of the sensors and the number of sensors. Often, many sensors are required to be placed in a room to achieve sufficient spatial resolution [11]. The second aspect is simulation modelling calculations; CFD has been widely used to predict the spatial variation of indoor environmental variables [14], but the large amount of computation time makes real-time prediction extremely difficult and real-time control unlikely.

The time-splitting method for solving the continuity equation and the non-deterministic Navier–Stokes equation can overcome the problems of large computational effort. Liu, W et al. [15] proposed a fast calculation using the free-form deformation (FFD) model. Although the calculation time is substantially reduced, the implementation is still computationally expensive, especially for real-time control. Unlike the CFD and FFD models, partitioning models are easy to incorporate into control systems [16] and require very minimal computational time as they only solve the energy and mass balance equations for each thermal zone. However, assuming all quantities in each partition are homogeneous, the partition model does not provide detailed spatial information about the room space [17]. The third category is data-driven methods, which use large amounts of data to obtain reasonable conclusions through a series of machine learning iterations. ANNs are one of the most widely used data-driven methods for rapid estimation of indoor environments [18–21]. ANNs are trained to model non-linear relationships between boundary conditions and environmental variables by training data obtained from CFD simulations. However, ANN models can easily be over fitted [11]. In addition, and more importantly as a black box model, interpreting the results predicted by the ANN model is difficult. Therefore, with the continuous development of computer technology, a series of new data processing methods have emerged, among which data dimensionality reduction methods to reduce the amount of data processing and deep learning methods from a large amount of data deep laws have been rapidly developed, of which the most well-known and widely used is the Principle Component Analysis (PCA), also often called the POD method.

The POD method enables rapid acquisition of flow fields by constructing reduced dimensional models. Hotelling H [22] begins by deriving the mathematical principles of the POD method, the idea of which is to reduce the dimensionality of the data by extracting the main information from the matrix. Simulate the flow field by computational fluid dynamics with known environmental parameters or boundary parameters to form a high-dimensional flow field data set and to project the high-dimensional data set into a low-dimensional space. By solving the eigenvectors and eigenvalues of the covariance

matrix to construct several linearly independent orthogonal bases, the flow field under any design parameter can be represented as a linear combination of the orthogonal bases and their corresponding coefficients, enabling the rapid acquisition of the downscaled and flow fields from the original data. As an important tool for data dimensionality reduction, POD methods are widely used in data mining, machine learning, signal processing, image recognition and other fields.

The POD method was first introduced in the field of turbulence by Bakewell [23] in 1967, and then Sirovich et al. [24] introduced ‘snapshots’ to the POD method, addressing the difficulty of solving the POD modes due to their high dimensionality. Since then, the POD method has been widely used. The greatest advantage of the POD method is that it can capture the vast majority of the flow characteristics in the physical field using only a few limited POD groups [25]. Li [26] et al. proposed a combination of POD and surface interpolation to construct a four-parameter model containing temperature, airflow, concentration and PMV distribution, which can be used to quickly obtain information about the indoor environment and thus improve ventilation methods to improve comfort and reduce energy costs. In order to verify the predictive effectiveness of the POD method, Li et al. [27] further built a model and embedded the POD method into a Proportional-Integral-Derivative (PID) controller for testing, and the results showed that the control accuracy of the method was acceptable. Ghosh et al. [28] used the POD method to build a downscaled model of a data centre for the rapid prediction of the temperature distribution in the data centre. Sha [29] used the greenhouse environment as the research object, used the CFD method to obtain temperature field information, applied the POD method to reconstruct the indoor environmental temperature field with parameter variation and used CFD to verify its accuracy. In terms of parameter design, Elhadidi and Khalifa [30] used the POD method to predict the velocity and temperature distribution in an empty office, optimising parameters such as the air supply velocity and air supply temperature of the room. The above literature shows that the method is computationally efficient and accurate by building a reduced dimensional model to predict fluid flow and design optimal parameters.

However, cases such as sudden source changes can lead to missing environmental or boundary parameters, hampering projecting the flow field directly using the POD. To solve this problem, Everson and Sirovich [31] proposed the gappy POD method, which introduces finite sensor measurements into the POD framework by defining the known sensor position information as a mask matrix, and new modal coefficients, which are then linearly combined with the modalities to reconstruct the flow field, can be combined by calculating the mask matrix. Based on the gappy POD method, JingLei [32] et al. proposed the combination of numerical simulation information and measurement information to reconstruct the stable temperature field from local measurement data and verified its feasibility and effectiveness by numerical simulation. Sun et al. [33] proposed a real-time reconstruction of physical fields by fusing CFD information into the gappy POD algorithm, which has a large reconstruction range and high accuracy. Tsering Xiao [34] et al. used the gappy POD method to estimate missing data in Tibetan weather forecasts. Numerous studies have demonstrated the ability of gappy POD to reconstruct the flow field rapidly and accurately when combined with measurements from a limited number of sensors for a given set of POD modes. Gappy POD has performed well in turbulence [35], wing detection [36,37] and ship operations [38], but few studies have applied gappy POD to the design of indoor environmental parameters, and validation analysis of this method is lacking.

In summary, most existing methods for creating non-uniform environmental fields are based on CFD to obtain physical field information under different design parameters, which requires a significant amount of time and computational resources. There is therefore an urgent need to find a method to speed up the acquisition of physical fields while ensuring the accuracy of the results and to ensure that the flow field information can be reconstructed quickly and accurately even when environmental parameters or boundary parameters

are missing, and the gappy POD method performs well in this respect. Therefore, this paper proposes an optimisation scheme targeting different demands at varied locations within the same room, where multiple design variables are simultaneously optimised from the perspective of complete and missing boundary parameters. Then, the reliability of the method is verified by building an artificial environment chamber. The result is a rapid adjustment of the design parameters of the air conditioning system, thus providing a theoretical approach to the creation of an efficient non-uniform environment.

## 2. Methods

### 2.1. Principle of POD Reconfiguration

The POD method is an efficient means of linearly reducing the dimensionality of the data. The data can be centred at the beginning, which translates all vector intercepts to the origin, thus guaranteeing that different vectors can be compared directly with one another. According to the relevant literature [39–41], the POD method is derived as follows:

The vector transformation is shown in Equation (1):

$$\mathbf{u}_i = \mathbf{x}_i - \bar{\mathbf{x}} \quad (1)$$

where  $\mathbf{u}_i$  is the decentralised vector;  $\mathbf{x}_i$  is the actual extracted vector; and  $\bar{\mathbf{x}}$  is the mean value of a vector.

Each set of flow field vectors  $\mathbf{u}_i$  corresponds to a unique boundary parameter  $Q$ , and multiple changes of boundary conditions form the required matrix  $U$ . The sample data consisting of the matrix  $U$  are processed to obtain an intrinsic orthogonal basis  $\{\varphi_i\}_{i=1}^L$ , also known as the POD mode, which can best represent the full range of information about the working flow field. It can also be interpreted as the maximum of the projection of any vector  $\mathbf{u}_i$  in the matrix  $U$  onto the set of eigenorthogonal bases, as shown in Equation (2):

$$\frac{1}{M} \sum_{k=1}^M \langle \mathbf{U}^j, \mathbf{U}^k \rangle > \mathbf{a}_k^i = \lambda_i \mathbf{a}_i^j, \quad (j = 1, 2, \dots, M) \quad (2)$$

where  $\lambda_i$  is the eigenvalue of the sample self-covariance matrix, ranked in descending order in terms of the size of the included energy (i.e., the size of the actual value).

$$\varphi_k = \frac{\sum_{i=1}^n v_i \varphi_i^k}{\left\| \sum_{i=1}^n v_i \varphi_i^k \right\|} \quad (3)$$

where  $\varphi_k$  is all data of the sample (all modalities);  $v_i$  is the order of  $\lambda_i$  after rearrangement; and  $\varphi_i$  is the feature vector of each  $\lambda_i$ . Equations (4) and (5) show the mapping of arbitrary vectors onto the modalities:

$$\mathbf{U}^j = \sum_{i=1}^L \mathbf{b}_i^j \varphi_i \quad (4)$$

$$\mathbf{b}_i^j = \frac{\mathbf{U}^j \varphi_i}{\left\| \varphi_i \right\|^2} \quad (5)$$

where  $\mathbf{b}_i^j$  is the modal coefficient. Solving up to this point enables obtaining the modal coefficients corresponding to any set of parameters by difference and combining them linearly with the modal to obtain the predicted flow field data, as shown in Equation (6):

$$\mathbf{U}(q) = \sum_{i=1}^L \mathbf{b}_i \varphi_i + \bar{\mathbf{x}} \quad (6)$$

### 2.2. Principle of Gappy POD Reconstruction

The gappy POD method is an extension of the traditional POD method to handle incomplete or corrupted data collections. Gappy PODs are used to calculate new modal coefficients by combining the POD method with limited sensor data when the boundary

conditions or a boundary parameter are unknown. The specific theoretical steps for gappy POD can be obtained from the relevant literature [32,34,42], as follows:

Vector  $c \in U^N$  represents the room temperature field as a flow field. Each point  $p_k$  of the vector  $p$  represents the temperature value at the  $k$ -th grid point. The sensor data obtained with real-time feedback at several grid points  $k_1, k_2, \dots, k_q$ , where  $q$  is the number of sensors used for data measurement, are defined as a mask matrix, i.e., the matrix is processed into a matrix containing only sensor position information, as shown in Equation (7):

$$E = (e_{k_1}, e_{k_2}, \dots, e_{k_q}) \in \mathbb{R}^{n \times q} \quad (7)$$

where  $e_k$  is the  $k$ -th unit vector. Equation (8) facilitates the formation of a known concentration vector:

$$E^T p = (p_{k_1}, p_{k_2}, \dots, p_{k_q})^T \quad (8)$$

The goal of gappy POD is to find new modal coefficients  $\tilde{b} \in \mathbb{R}^r$  using only the solution set containing the sensors, here defined as  $\tilde{\phi} \equiv E^T \phi \in \mathbb{R}^{q \times r}$ ,  $\tilde{p} \equiv E^T p \in \mathbb{R}^q$ . Then, Equation (9) is introduced.

$$\tilde{b} = \operatorname{argmin}_{\tilde{b} \in \mathbb{R}^r} \|\tilde{\phi} \tilde{b} - \tilde{p}\| \quad (9)$$

Equation (9) can be obtained using the least squares minimisation problem. The new  $\tilde{b}$  obtained by solving the equation is combined with the flow field information obtained from the previous calculation, i.e., the POD mode. The final new flow field is shown in Equation (10):

$$\tilde{U} \approx U(q) = \sum_{i=1}^L \tilde{b}_i \phi_i + \bar{x} \quad (10)$$

### 2.3. CFD Model

#### 2.3.1. Control Equations

##### Conservation of Mass Equation

All problems of flow are subject to the law of conservation of mass, and the equation of conservation of mass is also called the equation of continuity. It can be interpreted that the mass of all the fluid flowing into a micro-element per unit time is equal to the mass added to that micro-element per unit time, and its expression is shown in Equation (11)

$$\frac{\partial \rho}{\partial t} + \frac{\partial(\rho u)}{\partial x} + \frac{\partial(\rho v)}{\partial y} + \frac{\partial(\rho w)}{\partial z} = 0 \quad (11)$$

The gas flow in the model is incompressible viscous flow, and the air density and kinematic viscosity are constants. Thus,  $\frac{\partial \rho}{\partial t} = 0$ , then Equation (11) is deformed to the following equation:

$$\frac{\partial(\rho u)}{\partial x} + \frac{\partial(\rho v)}{\partial y} + \frac{\partial(\rho w)}{\partial z} = 0 \quad (12)$$

where  $\rho$ —Air density,  $\text{kg}/\text{m}^3$ ;  $t$ —Time,  $\text{s}$ ;  $u$ —Velocity vector component in  $x$ -direction;  $v$ —Velocity vector component in the  $y$  direction;  $w$ —Velocity vector component in the  $z$  direction.

##### Conservation of Momentum Equation

All problems of flow also follow the law of conservation of momentum, which is described as the rate of change of the momentum of a flow of a micro-element with respect to time being equal to all the combined external forces acting on that micro-element. It

is also an expression of Newton's second law. The equation expressions are shown in Equations (13)–(15):

$$\frac{\partial(\rho u)}{\partial t} + \text{div}(\rho u U) = -\frac{\partial p}{\partial x} + \frac{\partial \tau_{xx}}{\partial x} + \frac{\partial \tau_{yx}}{\partial y} + \frac{\partial \tau_{zx}}{\partial z} + F_x \quad (13)$$

$$\frac{\partial(\rho v)}{\partial t} + \text{div}(\rho v U) = -\frac{\partial p}{\partial x} + \frac{\partial \tau_{xx}}{\partial x} + \frac{\partial \tau_{yx}}{\partial y} + \frac{\partial \tau_{zx}}{\partial z} + F_y \quad (14)$$

$$\frac{\partial(\rho w)}{\partial t} + \text{div}(\rho w U) = -\frac{\partial p}{\partial x} + \frac{\partial \tau_{xx}}{\partial x} + \frac{\partial \tau_{yx}}{\partial y} + \frac{\partial \tau_{zx}}{\partial z} + F_z \quad (15)$$

where  $U$ —Combined speed, m/s;  $p$ —Static pressure, Pa;  $\tau_{ij}$ —Stress tensor, N/m;  $F_i$ —Forces acting on micro-elements, N.

### Conservation of Energy Equation

When a flow system contains heat exchange within it, the system must follow the law of conservation of energy, which falls under the first law of thermodynamics, which is described as the rate of increase of energy within the micro-element equal to the net heat flow into the micro-element plus the work done on the micro-element by the volume and surface forces. The expression for the conservation of energy equation is shown in Equation (16):

$$\frac{\partial(\rho T)}{\partial t} + \text{div}(\rho U T) = \text{div}\left(\frac{\lambda}{c_p} \text{grad} T\right) + S_T \quad (16)$$

where  $T$ —Thermodynamic temperature, K;  $\lambda$ —Thermal conductivity of air, W/(m·K);  $C_p$ —Specific heat capacity, J/(kg·K);  $S_T$ —The internal heat source of the fluid and the part of the fluid mechanical energy converted to heat due to viscous effects, referred to as the viscous dissipation term.

### 2.3.2. Physical Model

In this paper, a smaller scale model was built for the study, which has the dimensions of a 6 m × 6 m × 4 m (L × W × H) room, as shown in Figure 1. Inside the room, two sources of particle emission were selected, both with dimensions of 1 m × 1 m × 1 m (length × width × height). A total of 4 air outlets were arranged on both sides of the room, each with a corresponding size of 1 m × 0.1 m and with the bottom edge 0.4 m above the floor. The two air outlets on the same side were set up as a group. Four air vents were set up on the roof; the air vents were square, and the area was the same as the area of the air supply vents. The main object of study was selected as the breathing height of the personnel  $z = 1.5$  m.

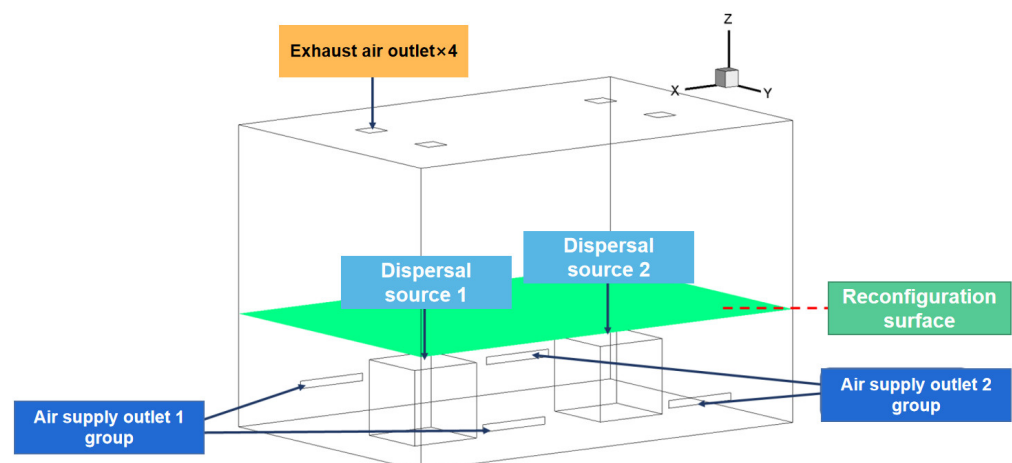


Figure 1. Schematic diagram of the physical model.

The numerical solution of the temperature field in this study was carried out using the commercial software Ansys Fluent 2021R1 (Ansys, Canonsburg, PA, USA). The acceleration due to gravity was set to  $g = -9.81 \text{ m/s}^2$ . Except for the pressure parameter discretization method, which was set to the staggered mesh PRESTO!, all other computation parameters were discretized using the second-order upwind scheme, and the numerical solution was solved using the SIMPLE algorithm. Since the airflow in the workshop was fully turbulent in terms of velocity and scale, a standard  $k - \varepsilon$  turbulence model was used.

In the standard  $k - \varepsilon$  turbulence model, the Reynolds stress is

$$-\rho \overline{u'_i u'_j} = \mu_t \left( \frac{\partial u_i}{\partial x_j} + \frac{\partial u_j}{\partial x_i} \right) - \frac{2}{3} \rho k \delta_{ij} \quad (17)$$

where the turbulent viscosity is

$$\mu_t = C_\mu \rho \frac{k^2}{\varepsilon} \quad (18)$$

Thus, the  $k$ -equation is introduced:

$$\frac{\partial}{\partial t}(\rho k) + \frac{\partial}{\partial x_i}(\rho k u_i) = \frac{\partial}{\partial x_j} \left[ \left( \mu + \frac{\mu_t}{\sigma_k} \right) \frac{\partial k}{\partial x_j} \right] + G_k + G_b - \rho \varepsilon - Y_M + S_k \quad (19)$$

And  $\varepsilon$  equation

$$\frac{\partial}{\partial t}(\rho \varepsilon) + \frac{\partial}{\partial x_j}(\rho \varepsilon u_j) = \frac{\partial}{\partial x_j} \left[ \left( \mu + \frac{\mu_t}{\sigma_\varepsilon} \right) \frac{\partial \varepsilon}{\partial x_j} \right] + C_{1\varepsilon} \frac{\varepsilon}{k} (G_k + G_{3\varepsilon} G_b) - C_{2\varepsilon} \rho \frac{\varepsilon^2}{k} + S_\varepsilon \quad (20)$$

In the equation,  $k = \frac{\overline{u'_i u'_i}}{2}$  is the turbulent kinetic energy;  $\mu + \frac{\mu_t}{\sigma_k}$  and  $\mu + \frac{\mu_t}{\sigma_\varepsilon}$  are the diffusivity of  $k$  and  $\varepsilon$ ;  $G_k$  is the turbulent kinetic energy due to the laminar velocity gradient;  $G_b$  is the turbulence due to buoyancy;  $Y_m$  is the turbulence due to diffusion;  $C_{1\varepsilon}$ ,  $C_{2\varepsilon}$  and  $C_{3\varepsilon}$  are constants; and  $S_k$  and  $S_\varepsilon$  are user-defined source terms.

$G_k$  is calculated by the formula

$$G_k = -\rho \overline{u'_i u'_j} \frac{\partial u_j}{\partial x_i} \quad (21)$$

$G_b$  is calculated as

$$G_b = \beta g_i \frac{\mu_t}{Pr_t} \frac{\partial T}{\partial x_i} \quad (22)$$

The values of the constants in the standard  $k - \varepsilon$  model are shown in Table 1:

**Table 1.** Standard model parameter values.

Coefficient	$C_{1\varepsilon}$	$C_{2\varepsilon}$	$C_{3\varepsilon}$	$\sigma_k$	$\sigma_\varepsilon$
Numerical	1.44	1.92	0.09	1.0	1.3

### 2.3.3. Boundary Condition Setting

CFD simulations require some reasonable settings in order to guarantee valid calculation results. In order to simplify the calculation model, the following assumptions are made:

- (1) The air can be assumed to be an incompressible flowing gas because the actual temperature, humidity and air flow rate are low in the industrial plant studied within the model;
- (2) The organization of the air in the model basin is in a steady state and turbulent, with the pressure varying continuously along the direction of flow;

- (3) The heat emitted by the two sources of emanation within the model is uniform and constant; the heat does not change as the amount of emanation fluctuates; and the walls do not take into account the effects of heat radiation;
- (4) Stable positive pressure inside the model, irrespective of the disturbances caused by infiltrating winds;
- (5) Ignore flow losses due to air viscosity.

The specific boundary condition settings and initial variable selections are shown in Table 2.

**Table 2.** Boundary conditions and initial variables.

Type	Types of Boundary Conditions	Parameter Settings	DPM
Air supply outlets	velocity-inlet	0.2 m/s~0.6 m/s	escape
Exhaust air outlet	pressure-outlet	/	escape
Dispersal source	wall	$c = 1 \times 10^{-8} \text{ kg/s} \sim 3 \times 10^{-8} \text{ kg/s}$ $T = 309 \text{ K}$	reflect
The rest of the envelope	wall	$T = 300 \text{ K}$	trap

#### 2.3.4. Gridding and Irrelevance Tests

Currently, grids can be divided into structural and unstructured and, of course, partially structured and partially unstructured. Structural meshes have a regular distribution and orderly node arrangement, while non-structural meshes are disordered and irregular. For the main objective of this paper, the model is divided into all structural meshes using ICEM-CFD2021 meshing software in order to facilitate the subsequent data processing, while the mesh is encrypted at the heat source walls to improve the calculation accuracy. The results of the grid division are shown in Figure 2.

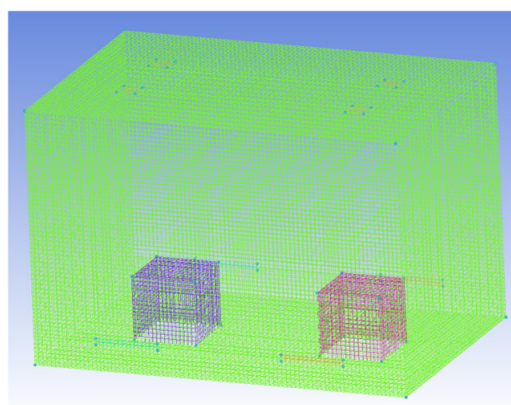


**Figure 2.** Schematic diagram of the grid division.

In order to determine the most appropriate grid size for the model in this paper, the global grid size was changed in ICEM-CFD using the function “Scale Factor”, which does not change the relative size of the grid and allows the grid encryption to remain constant. By adjusting the size of the parameter to change the mesh size, we obtained a model with mesh sizes of 102,046, 216,322, 441,284, 623,814 and 853,648, respectively. Comparing the relationship between the relative static pressure at the outlet and the number of meshes under the convergence condition, Figure 3 shows that when the number of meshes is greater than 623,814, the increase of meshes will basically have no effect on the simulation results, so the model with the number of meshes of 623,814 is finally determined as the numerical simulation of this paper.

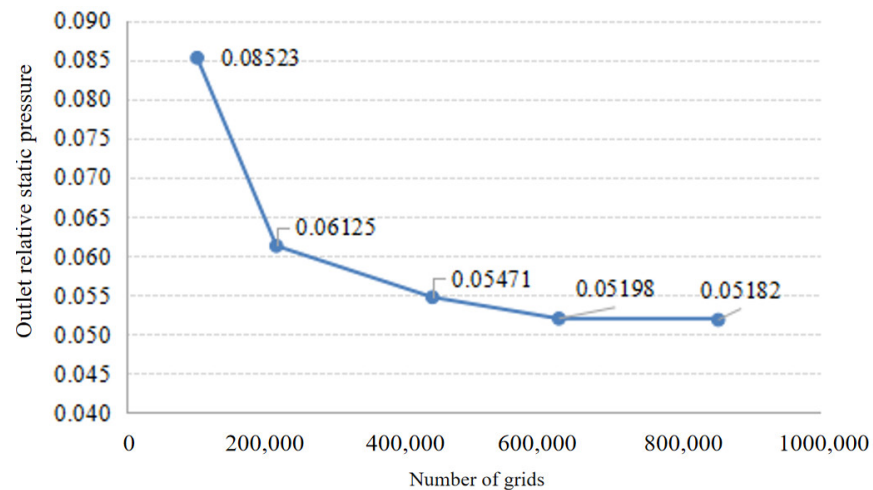


**Figure 3.** Comparison of relative static pressure at the outlet for different number of grids.

#### 2.4. Optimisation of Air Supply Parameters for Non-Uniform Temperature Fields

In the preset range of air supply parameters, the reconstructed value is compared with the target value, and the air supply parameter that corresponds to the smallest error between the two is the optimal air supply parameter that meets the design target. The optimisation formula is defined as follows:

$$E = \frac{1}{n} \sum_{i=1}^n |U_i - V_i| \quad (23)$$

where  $E$  is the average error;  $n$  is the number of reconstruction points selected, which is set to 4 in this paper.  $U_i$  is the reconstruction value of the  $i$ -th point, and  $V_i$  is the target value of the  $i$ -th point. Finding the optimum is to determine the air supply parameter with the smallest value of  $E$ .

Theoretically, the target points for the POD method can be any location and any number, so we arbitrarily chose two cases, each with four target points, to study.

As shown in Figures 4 and 5, four coordinate points (1, 1), (2, 2), (3, 3) and (4, 4) on the horizontal plane at  $z = 1.5$  m were selected as the demand position points for case one; coordinates (1, 3), (2, 3), (4, 1) and (5, 1) were selected as the demand position points for situation two.

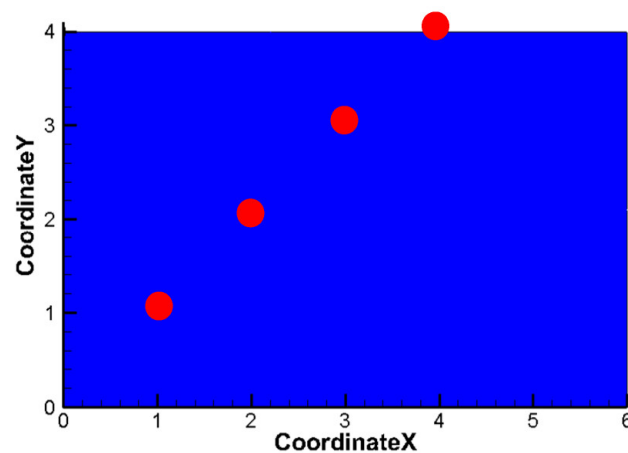


**Figure 4.** Situation 1 demand location points.

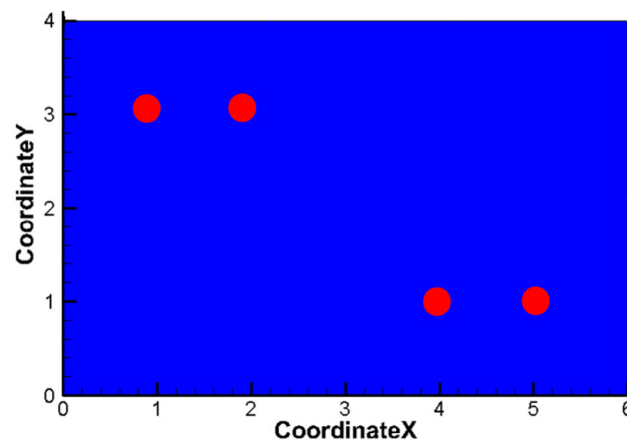


Figure 5. Situation 2 demand location points.

### 3. Analysis and Verification of Optimization Results

#### 3.1. Analysis of the Results of the Merit Search for Situation 1

Table 3 shows different target temperatures are set for each of the three sets of sample data, and the optimal solution of the air supply parameters was found through the written POD program.

Table 3. Target temperatures for each demand point.

Coordinates	(1, 1)	(2, 2)	(3, 3)	(4, 4)
Group 1 target temperature (K)	296.00	295.50	296.50	296.00
Group 2 target temperature (K)	297.50	296.50	297.00	297.50
Group 3 target temperature (K)	297.00	297.50	298.00	298.50

In this paper, the air supply parameters are optimised for the temperature demand generated at different locations for 9, 25 and 45 samples (considering a single parameter, two parameters and three parameters, respectively). Based on optimisation Equation (23), the POD optimisation procedure is used to filter the air supply parameters with the smallest error between the temperature reconstruction value at the demand point and its target value, and the optimisation results for each group are shown in Table 4.

Table 4. Optimisation results for the air supply parameters in situation 1.

Group	Merit Search Results
Group 1	T = 295.0 K
Group 2	T = 296.3 K, V = 0.37 m/s
Group 3	T = 296.3 K, V1 = 0.35 m/s, V2 = 0.46 m/s

Figure 6 shows the optimization of the air supply parameters for a single parameter, where the programmed temperature value at the demand point has the smallest deviation from the target temperature value of 0.36 K at a supply air temperature of 295.0 K. Figure 7 shows the optimization of the two parameters, where the temperature value calculated by the POD optimization program has the smallest average deviation from the target temperature value of 0.17 K at a supply air temperature of 295.0 K and a supply air velocity of 0.28 m/s. The minimum deviation from the target temperature value is 0.17 K. Similarly, the optimal air supply parameters obtained from the three-parameter search are air supply temperature 296.3 K, air supply velocity 0.35 m/s for air outlet 1 and 0.46 m/s for air outlet 2, with an average deviation of 0.11 K. The third set of samples contains three air supply parameters, which if plotted with the deviation values are four-dimensional images, which cannot be displayed as images at present.

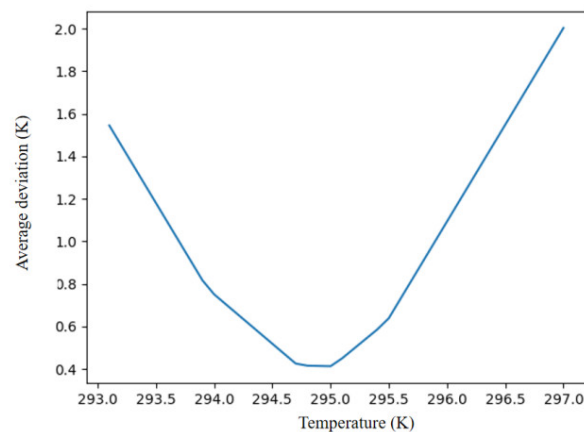


**Figure 6.** Error values for the first set of search results.

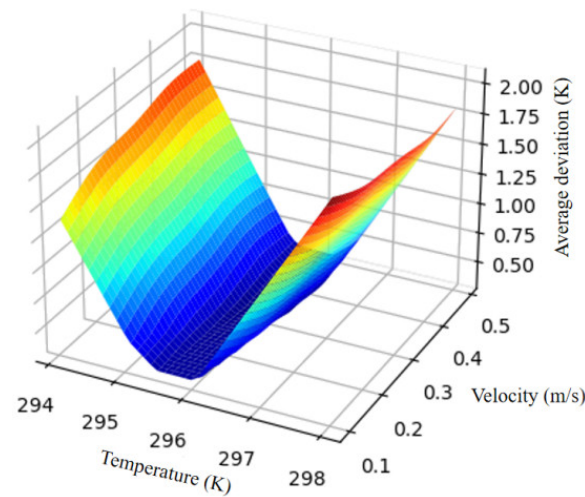


**Figure 7.** Error values for the second set of search results.

### 3.2. Analysis of the Results of the Merit Search for Situation 2

As shown in Table 5, on the basis of the demand point locations selected in Situation 2 (shown in Figure 5), different target temperatures were set for each of the three sets of sample data, and their air supply parameters were individually sought by the POD program that had been written in order to create a non-uniform temperature field that met the demand.

**Table 5.** Situation 2 target temperature.

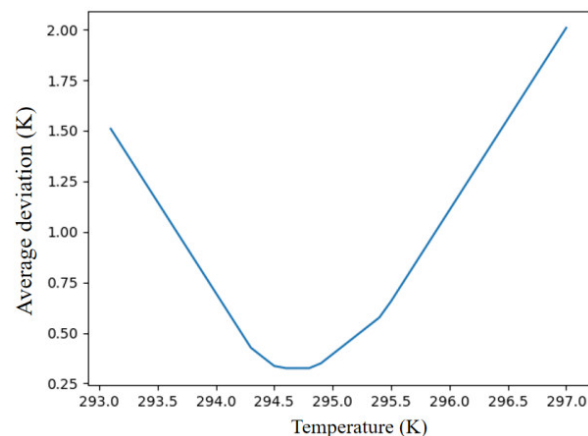
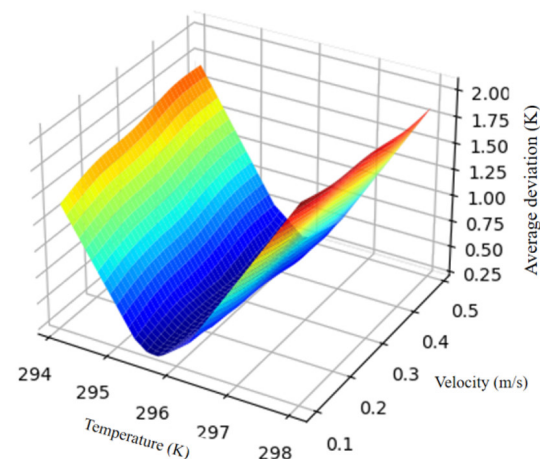
Coordinates	(1, 3)	(2, 3)	(4, 1)	(5, 1)
Group 1 target temperature (K)	296.0	295.5	296.5	296
Group 2 target temperature (K)	297.5	296.5	297.0	297.5
Group 3 target temperature (K)	299.5	299.0	298.5	298.0

According to the target temperatures set in Table 3 for the three groups of samples, the air supply parameters with the smallest error between the reconstructed temperature value at the demand point and its target value were selected using the POD search procedure according to the optimisation formula, and the results of each group are shown in Table 6.

**Table 6.** Optimisation results for the air supply parameters in situation 2.

Groups	Merit Search Results
Group 1	T = 294.7 K
Group 2	T = 295.8 K, V = 0.10 m/s
Group 3	T = 296.5 K, V1 = 0.15 m/s, V2 = 0.26 m/s

Figure 8 shows the first group of air supply parameter finding, when the supply air temperature is 294.7 K, and the programmed temperature value at the demand point has the smallest deviation from the target temperature value of 0.31 K. Figure 9 illustrates the second group of the optimization search, when the air supply temperature is 295.8 K, and the air supply speed is 0.10 m/s; the temperature value calculated by the POD optimization program has the smallest average deviation from the target temperature value, with a deviation of 0.15 K. Similarly, the optimal air supply parameters obtained from the third group of the optimization search are as follows: air supply temperature 296.5 K, air supply speed 0.15 m/s for air outlet 1, air supply speed 0.26 m/s for air outlet 2, with an average deviation of 0.09 K. As the third group of samples contains three air supply parameters, it is also not possible to show the average deviation in relation to the air supply parameters in images. The mean deviation was 0.09 K. As the sample of the third group contained three air supply parameters, it was also not possible to show the relationship between the mean deviation and the air supply parameters in an image.

**Figure 8.** Error values for the first set of search results.**Figure 9.** Error values for the second set of search results.

### 3.3. Validation of Optimization Results for Situation 1

Figures 10–12 show the CFD simulation results as simulation conditions. The temperature values of each demand point are extracted and compared with the target temperature, as shown in Table 7. The errors are calculated and evaluated to verify the reliability of the CFD + POD method by comparing the target temperature value of the demand point with its simulated temperature value.

The error equation is defined as follows:

$$E = \frac{|T_{CFD} - T_{tar}|}{T_{tar} - 273.15} \quad (24)$$

where  $T_{CFD}$  is the CFD simulated temperature value, and  $T_{tar}$  is the target temperature value at the demand point.

The average deviations for the first, second and third groups are 0.405 K, 0.368 K and 0.380 K, respectively, with average errors of 1.79%, 1.55% and 1.47%, respectively. The deviation of the demand point (4, 4) in the first group of samples is only 0.05 K, with an error as low as 0.22%. For all samples, the demand point (2, 2) deviates slightly from the target temperature value because it is directly above the heat source, and objectively achieving a low temperature demand at this point is more difficult. Overall, the simulated temperature values under the search results are closer to the target temperature values at this point, indicating the search design based on the CFD + POD method can meet the multiposition requirements for non-uniform temperature fields.

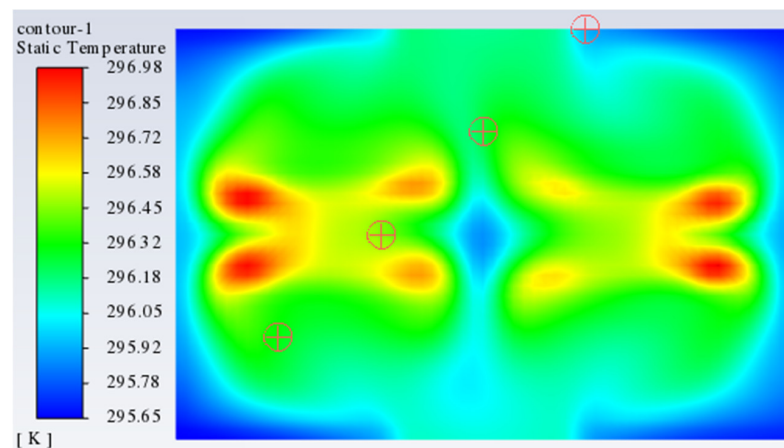


Figure 10. Verification of the first set of search results.

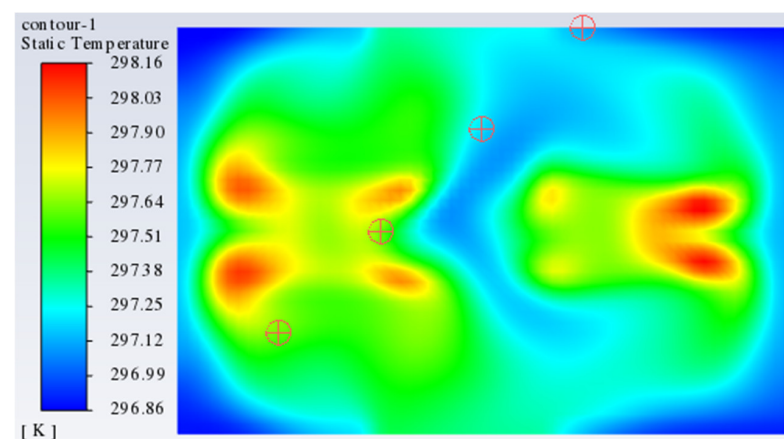


Figure 11. Verification of the second set of search results.

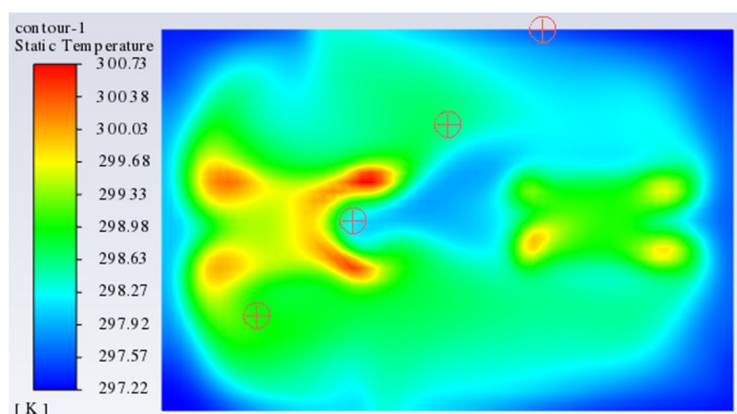


Figure 12. Verification of the third set of search results.

Table 7. Optimization verification results for each location point.

Group	Demand Point Coordinates	(1, 1)	(2, 2)	(3, 3)	(4, 4)
Group 1	Target temperature (K)	296.00	295.50	296.50	296.00
	Simulated values (K)	296.31	296.46	296.20	295.95
	Deviation (K)	0.31	0.96	0.30	0.05
	Error	1.36%	4.30%	1.28%	0.22%
Group 2	Target temperature (K)	297.50	296.50	297.00	297.50
	Simulated values (K)	297.62	297.28	297.20	297.13
	Deviation (K)	0.12	0.78	0.20	0.37
	Error	0.49%	3.34%	0.84%	1.52%
Group 3	Target temperature (K)	299.50	299.00	298.50	298.00
	Simulated values (K)	299.05	298.29	298.64	297.78
	Deviation (K)	0.45	0.71	0.14	0.22
	Error	1.71%	2.75%	0.55%	0.89%

### 3.4. Validation of Optimization Results for Situation 2

Similarly, Figures 13–15 show the temperature values of each demand point and the temperature field of the entire surface in situation 2. The temperature values of each demand point are extracted and summarized with the target temperature in Table 8. After changing the demand point locations, the target temperature and simulated temperature are compared, and the error is calculated using Equation (24). The average deviations for the first, second and third groups were 0.440 K, 0.433 K and 0.400 K, respectively, and the average errors were 1.93%, 1.81% and 1.55%, respectively. These values were relatively small, which confirms the correctness of the optimization results and proves that the CFD + POD method can design the optimal air supply scheme for any demand point. Combined with situation 1, the feasibility of this method for creating any non-uniform temperature field is demonstrated.

Table 8. Optimization verification results for each location point in case 2.

Groups	Demand Point Coordinates	(1, 3)	(2, 3)	(4, 1)	(5, 1)
Group 1	Target temperature (K)	296.00	295.50	296.50	296.00
	Simulated values (K)	296.25	296.36	295.96	296.11
	Deviation (K)	0.25	0.86	0.54	0.11
	Error	1.09%	3.85%	2.31%	0.48%
Group 2	Target temperature (K)	297.50	296.50	297.00	297.50
	Simulated values (K)	296.95	297.21	297.13	297.16
	Deviation (K)	0.55	0.71	0.13	0.34
	Error	2.26%	3.04%	0.55%	1.40%
Group 3	Target temperature (K)	299.00	298.00	298.50	297.50
	Simulated values (K)	299.88	299.41	298.69	298.60
	Deviation (K)	0.38	0.41	0.19	0.60
	Error	1.44%	1.59%	0.75%	2.41%

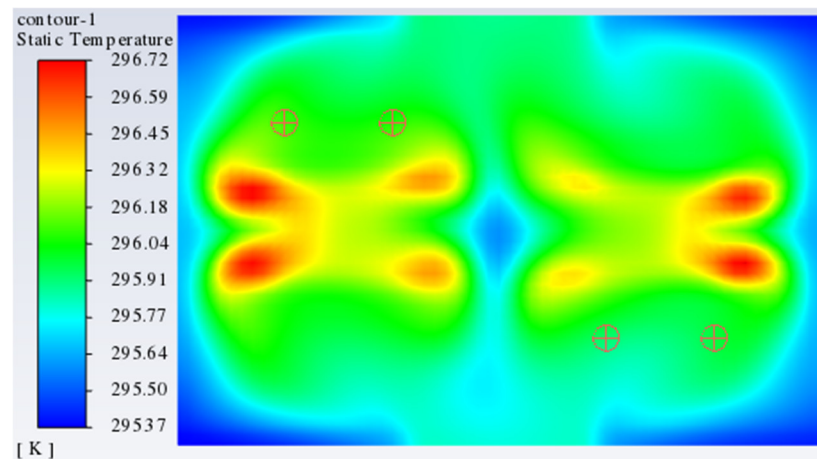


Figure 13. Verification of the first set of search results.

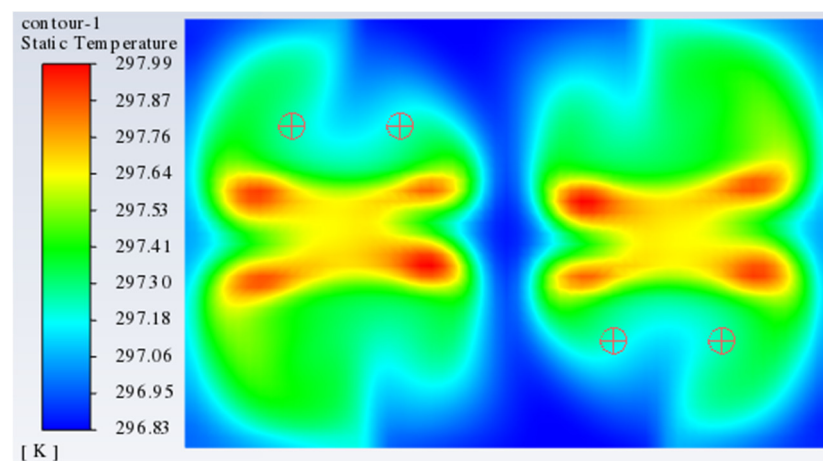


Figure 14. Verification of the second set of search results.

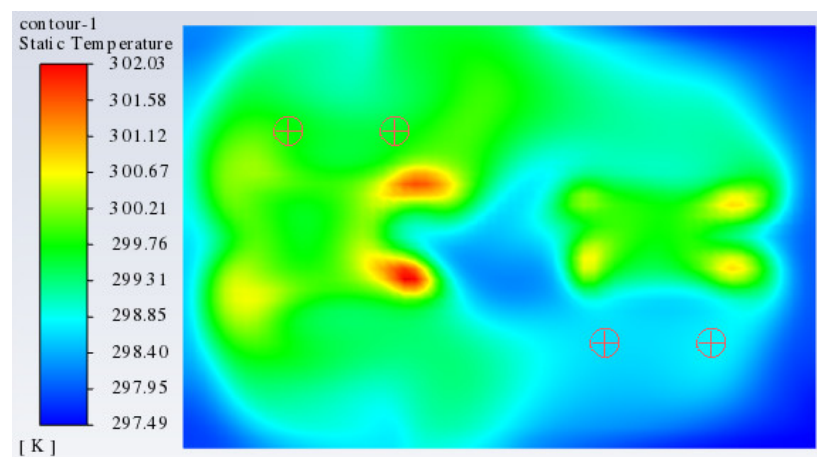


Figure 15. Verification of the third set of search results.

#### 4. Experimental Verification

Based on the above research methods, the temperature field is quickly reconstructed with the aid of a computer program, and a target temperature is set for any point based on the available data samples to filter out the optimum air supply parameters to meet the target. Theoretically, the accuracy of the POD reconstructed flow field depends on the CFD data, which can be used to validate the POD reconstructed field data if the CFD data

accuracy can be met. However, to ensure the engineering reliability of the design method, the accuracy of the POD method must be repeatedly verified to reconstruct the flow field. Therefore, this paper builds an artificial environment chamber to validate experimentally the POD-seeking method of creating a non-uniform temperature field.

#### 4.1. Test Bench Construction

The laboratory measures  $2.8 \times 2.5 \times 2.2$  m (L  $\times$  W  $\times$  H) and is equipped with an air conditioning system to ensure a stable indoor environment. The dimensions of the artificial environment chamber are  $2 \times 1 \times 1$  m (L  $\times$  W  $\times$  H), as shown in Figure 16:

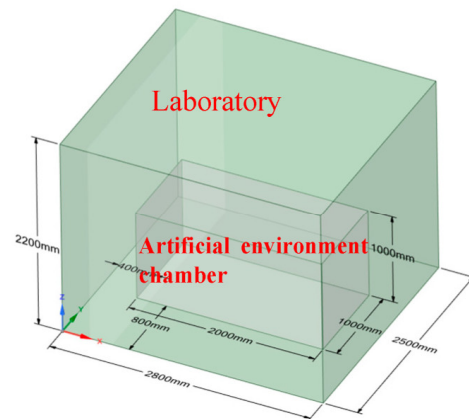


**Figure 16.** Schematic diagram of the experimental platform.

In this experiment, the cooling water tower is used as the cooling source, and the air supply system is an integral air conditioning unit (AHU). The maximum air volume of the fan is  $80 \text{ m}^3/\text{h}$ , with variable frequency regulation. The test rig is made of 50 mm thick polyurethane insulation panels, and the top is made of acrylic glass panels to allow easy observation of the interior of the chamber. The laboratory table is internally arranged with two cast aluminium heating plates as heat sources, with dimensions of  $100 \times 100 \times 20$  mm (L  $\times$  W  $\times$  H). The heating power is regulated by means of a transformer, and the power range is 0–300 W. The two sides of the test bench are arranged with two air supply outlets, for a total of four, and the air outlet size is  $150 \times 150$  mm. The top of the test bench is arranged with two return air outlets; the return air outlet size is  $200 \times 200$  mm, and the specific location as shown in Figure 17.

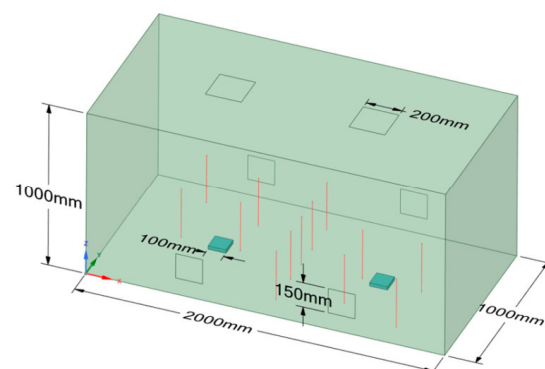


**Figure 17.** Schematic diagram of the internal structure of the experimental chamber.

The test bench is made of insulated panels bonded by structural adhesive, with patching done at the junction and the top acrylic panel sealed by aluminium foil tape, as shown in Figure 18.



**Figure 18.** Schematic diagram of the test stand.

The temperature sensor is fixed to the top of a 3 mm diameter stainless steel bar, which is fixed to the bottom of the test bench by means of a guide fixing base, as shown in Figure 19. Temperature sensors need to be calibrated for accuracy before use. All temperature sensors are placed in a thermostat. The set temperature of the thermostat is used as the standard. A set of data is read every 15 s. After 1 h and after the sensor temperature value has stabilised, the average value of the data within 2 min after stabilisation is taken as the measurement result. The measurement result is compared with the set temperature, as shown in Figure 20. The temperature sensor is selected for this experiment. The average deviation is 0.045 °C, and the maximum deviation is not more than 0.2 °C, which meets the accuracy requirement.



**Figure 19.** Guided fixing base with stainless.

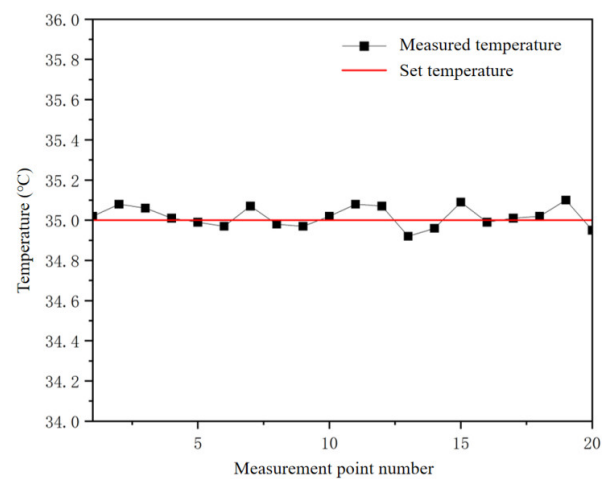


**Figure 20.** Temperature sensor calibration results steel bar for fixing measurement points.

#### 4.2. Experimental Programme

This experiment entails validation. The horizontal plane with  $z = 0.3$  m height and the vertical plane with  $x = 1.25$  m is selected as the validation plane, as shown in Figure 21. The measurement points are arranged on these two planes. Firstly, the data obtained from the measurement points are compared with those obtained from the POD reconstruction through the experiment, and several demand points are selected on the 0.3 m horizontal plane. The target temperature is defined for them, and the best air supply parameter is calculated through the two reconstruction methods. The air supply parameters are then used as the experimental conditions to obtain the measured temperature at the target point and compare it with the target temperature.

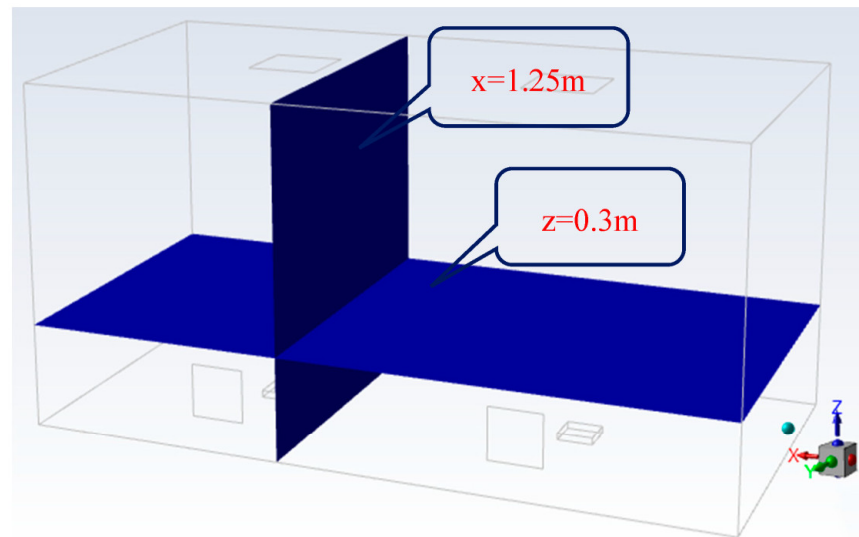


Figure 21. Diagram of the verification surface.

##### 4.2.1. Location of Measurement Points

The points are arranged with reference to the diagonal principle, with thirteen points in the horizontal plane at  $z = 0.3$  m and seven points in the vertical plane at  $x = 1.25$  m. The layout of the measurement points is shown in Figures 22 and 23.

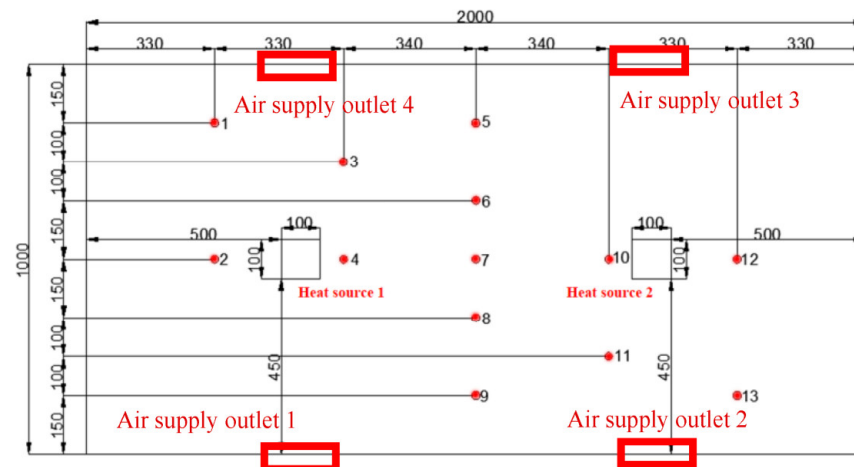
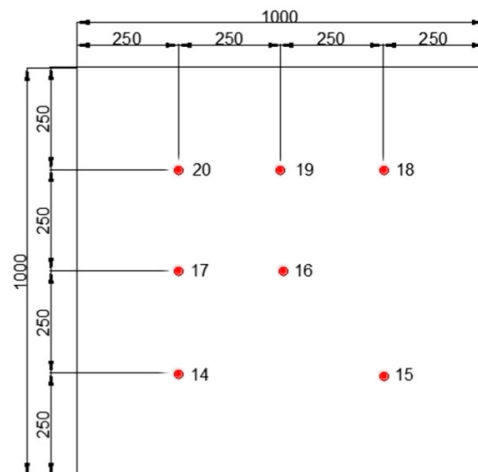


Figure 22. Layout of measurement points at  $z = 0.3$  m Unit: mm.



**Figure 23.**  $x = 1.25$  m measurement point layout.

#### 4.2.2. Experimental Working Conditions

The experiment is divided into four steps. The first step experiment verifies the accuracy of the CFD simulation. The second step experiment tests the precision of the POD reconstruction data. The third step experiment verifies the accuracy of the POD search results. The fourth step experiment verifies the accuracy of the gappy POD reconstruction data.

- (1) The first step is to verify the accuracy of the CFD simulation by building a CFD model exactly according to the test bench and setting up four working conditions to verify whether the CFD simulated temperature matches the measured temperature. Taking work conditions 1 as a reference, the power source 2 increases the heat source to 64 W; operating conditions 3 reduce the air supply temperature to 19 °C; and operating conditions 4 reduce the air supply speed to 0.2 m/s. The experimental boundary parameters are shown in Table 9.
- (2) The second step is to verify the accuracy of the POD reconstruction data. Firstly, 27 data samples are obtained by CFD simulation. The wind speed is taken at 0.1 m/s intervals, and the air supply temperature is taken at 1 °C intervals. The simulated working conditions are shown in Table 10. The sample characteristics are extracted, and the temperature field under a certain boundary condition is reconstructed. Finally, the experimental values of twenty measurement points under this boundary condition are compared with the corresponding reconstructed values.

**Table 9.** The measured air supply parameters and thermal source power of the first group of experiments.

Work Conditions	Air Supply Temperature (°C)	Air Supply Speed (m/s)	Heat Source Power (W)
1	21	0.3	36
2	21	0.3	64
3	19	0.3	36
4	21	0.2	36

**Table 10.** CFD simulations for 27 data samples.

Air Velocity at Air Supply Ports 1 and 2 (m/s)	Air Velocity at Air Supply Ports 3 and 4 (m/s)	Air Supply Temperature (°C)	Heat Source Power (W)
0.1~0.5	0.1~0.5	19~21	36

In this paper, any two target operating conditions are selected for reconstruction within the interval of air supply parameters of the above 27 data samples (see Table 11), and then the air supply parameters of these two target operating conditions are used as experimental conditions for the experiments. After the temperature in the experimental chamber has stabilised, the temperature values of 20 measurement points are extracted and compared with the reconstruction results under these location points.

**Table 11.** Target operating conditions reconstructed based on the POD method.

Boundary Conditions	Air Velocity at Air Supply Ports 1 and 2 (m/s)	Air Velocity at Air Supply Ports 3 and 4 (m/s)	Air Supply Temperature (°C)	Heat Source Power (W)
Reconstructed working condition 1	0.2	0.3	20.5	36
Reconstructed working condition 2	0.25	0.15	19.5	36

- (3) The third step is to verify the reliability of the POD-based method. In this paper, three points on the horizontal plane at  $z = 0.3$  m inside the test rig are selected as demand points, namely points 5, 7 and 9 (see Figure 24). The air supply parameters are optimised for a given target temperature at the demand point, and then the optimisation results are used as the experimental conditions to compare and analyse the error between the measured temperature at the demand point and its target value, thus demonstrating the POD method can effectively create a non-uniform temperature field.

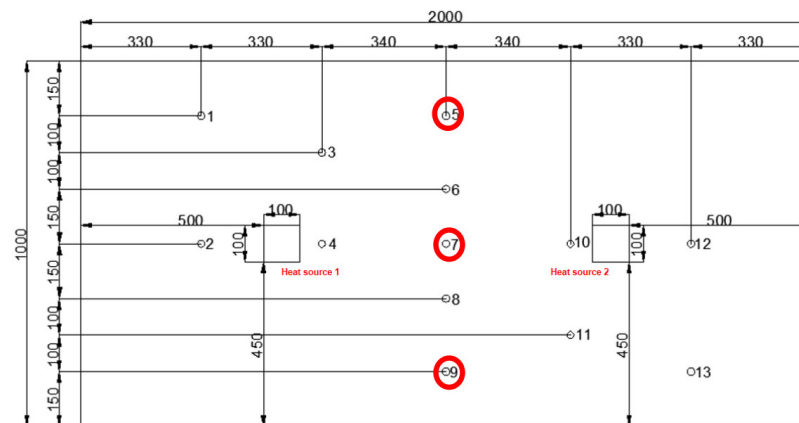


**Figure 24.** Schematic diagram of the internal demand points.

- (4) The fourth step is to verify the accuracy of gappy POD reconstruction data. The experimentally obtained temperature values of thirteen measurement points in the  $z = 0.3$  m plane are divided into two groups. Measurement points 4, 5, 7 and 10 comprise the control group, and the rest of the points are used as the input values of gappy POD. The distribution of the measurement points is shown in Figure 25. The error calculation is still carried out as in Equation (11), where  $t_{CFD}$  is replaced by  $t_{cal}$ . The result of the gappy POD calculation and working conditions 1 and working conditions 3 in the experimental validation are selected for comparison.

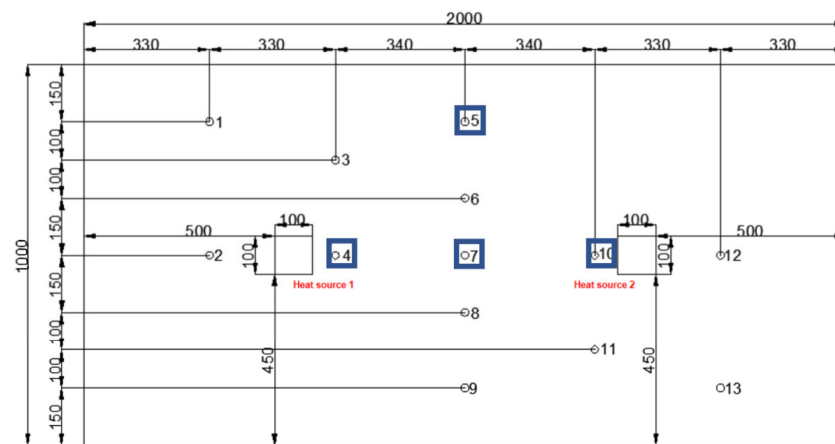


Figure 25. Diagram of test point selection and allocation of the test bench.

## 5. Results and Discussions

Figure 26 shows the experimental system is adjusted at 16:30, and the system could reach a stable state again after about 90 min. The experimental data collection interval is 15 s, and the experimental parameters are continuously adjusted with the above test conditions as the target. After the internal environment of the experimental chamber has stabilised, the average temperature within 5 min is taken as the final experimental value, and the statistics of the experimental values are summarised as follows.

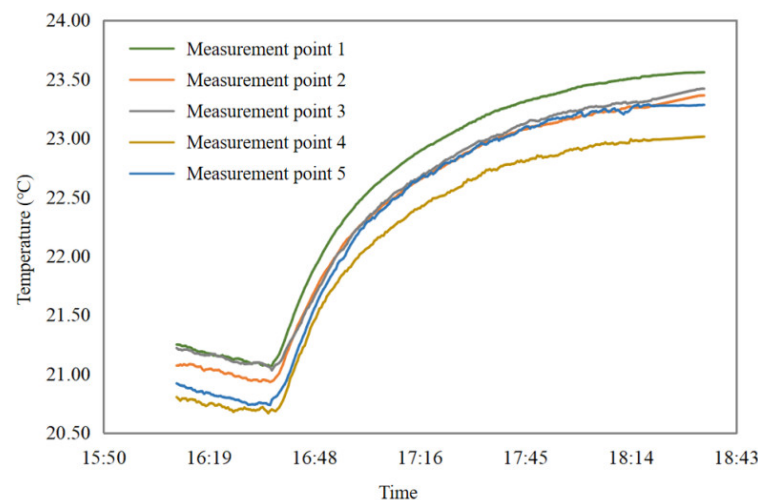


Figure 26. Process of temperature change at some measurement points.

### 5.1. Comparison of Experimental Results with Simulation Results

The experiments are carried out according to the working conditions listed in Table 4, and the temperature values of twenty measurement points (see Figures 22 and 23) are extracted after the internal temperature of the test rig had stabilised. The results of CFD simulations are summarised in Table 12. The error  $\sigma$  between the simulated and measured temperatures is defined as follows:

$$\sigma = \frac{t_c - t_m}{t_c} \times 100\% \quad (25)$$

The average errors for the four operating conditions are 2.15%, 3.42%, 2.79% and 1.33%, as shown in Figures 27–30. There is a high degree of agreement between the simulated temperature and the measured temperature. Conditions 1, 2 and 3 in the experimental adjustment finds that the air outlets 1 and 2 wind speed is high (about 0.1 m/s higher than

air outlets 3 and 4), as shown in Figure 22. Air outlet 1 is facing the measurement point 4. When the wind speed is larger, although point 4 is close to the heat source, its cooling effect is better, so the temperature value is not high, whereas point 2 is offset from the position directly opposite the air supply opening, and the distance to the heat source is closer, so the temperature of point 2 is high. When the air velocity of air supply outlet 2 becomes high, the cold air blows directly into the central area of the experimental chamber, resulting in point 13 being in the dead centre of the air supply, so the temperature at this point is also higher. The temperature values at measurement points 2 and 13 are slightly in error with the simulated results by approximately 7%.

**Table 12.** Experimental data and numerical simulation calculation error results.

Measurement Points	1	2	3	4	5	6	7	8	9	10
Condition 1	2.14%	7.77%	0.93%	3.24%	2.47%	1.25%	0.06%	0.14%	0.53%	0.89%
Condition 2	2.04%	11.63%	2.47%	3.69%	5.33%	3.54%	1.41%	0.90%	1.25%	4.88%
Condition 3	2.19%	8.15%	1.36%	3.39%	3.33%	1.57%	0.60%	1.37%	2.27%	0.78%
Condition 4	0.32%	0.72%	1.16%	1.99%	0.65%	2.17%	0.65%	0.17%	0.15%	0.36%
Measurement points	11	12	13	14	15	16	17	18	19	20
Condition 1	2.19%	2.02%	7.43%	1.33%	0.62%	1.05%	1.12%	2.99%	2.43%	2.48%
Condition 2	2.58%	5.13%	11.83%	1.83%	0.82%	2.70%	2.43%	5.77%	4.85%	4.93%
Condition 3	3.20%	4.37%	8.79%	2.19%	1.00%	1.32%	1.16%	4.50%	2.65%	1.59%
Condition 4	0.35%	1.83%	1.30%	0.66%	2.32%	0.19%	1.95%	3.42%	2.39%	3.82%

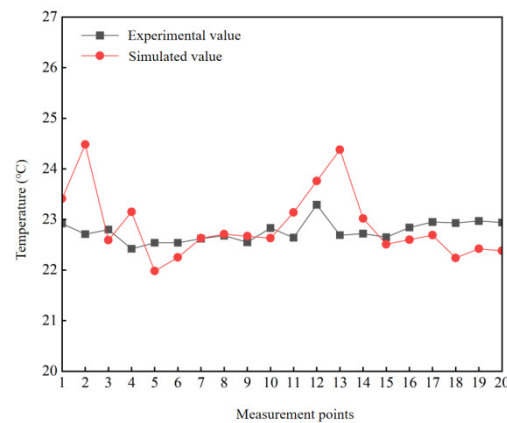


**Figure 27.** Comparison of experimental simulations for working condition 1.

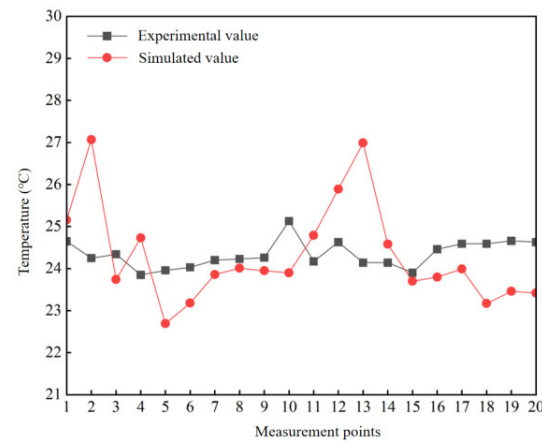


**Figure 28.** Comparison of experimental simulations for working condition 2.

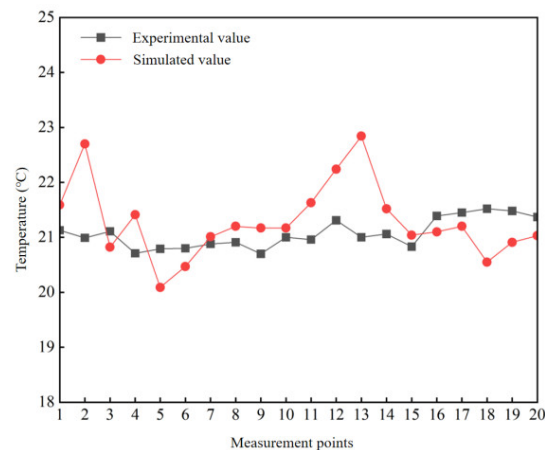


Figure 29. Comparison of experimental simulations for working condition 3.

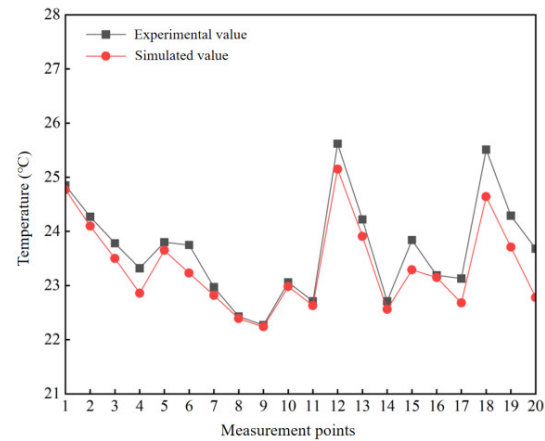


Figure 30. Comparison of experimental simulations for working condition 4.

Conditions 1, 2 and 3 are CFD simulations according to the set conditions (Table 4). The experiments are still conducted under these conditions. The air supply parameters of each air outlet have varying degrees of minor deviations from the set working conditions. Working condition 4 is tested by first adjusting the experimental parameters and then using the measured air supply parameters as simulation conditions, which is mainly why working condition 4 is more accurate than 1, 2 and 3. The measured air supply parameters for each air supply outlet are shown in Table 13.

Table 13. Deviation of measured air supply parameters from set values for each air supply outlet.

Working Condition	Set Working Condition	Air Supply Temperature (°C)				Air Supply Speed (m/s)			
		Air Supply Outlet 1	Air Supply Outlet 2	Air Supply Outlet 3	Air Supply Outlet 4	Air Supply Outlet 1	Air Supply Outlet 2	Air Supply Outlet 3	Air Supply Outlet 4
1	Temperature 21 °C;	21.2	20.9	21.1	21.1	0.36	0.37	0.30	0.29
	wind speed 0.3 m/s Deviation (°C, m/s)	0.2	0.1	0.1	0.1	0.06	0.07	0.00	0.01

### 5.2. Comparison of Experimental Results with Reconstructed Results

Based on the 27 data samples obtained from the CFD simulations, the temperature fields on the horizontal plane at  $z = 0.3$  m and the vertical plane at  $x = 1.25$  m are reconstructed using the POD method according to the working conditions set in Table 6. The

experiments are also carried out according to the working conditions in Table 6, compared with the temperature values of the corresponding 20 location points on the reconstructed surface and the error values are calculated according to Equation (25), where  $t_m$  is the reconstructed value, and the results are shown in Tables 14 and 15.

**Table 14.** Comparison of experimental data and reconfiguration results (reconfiguration condition 1).

Measurement Points	1	2	3	4	5	6	7	8	9	10
Experimental data (°C)	24.03	23.82	23.53	23.44	23.62	23.54	23.49	23.45	23.69	24.07
Reconstructing data (°C)	24.38	22.85	22.77	22.16	22.99	22.97	22.94	22.92	22.31	22.03
Error	1.46%	4.07%	3.24%	5.46%	2.70%	2.43%	2.36%	2.25%	5.83%	8.46%
Measurement points	11	12	13	14	15	16	17	18	19	20
Experimental data (°C)	23.60	24.10	23.67	23.66	23.64	24.04	24.00	23.97	24.08	23.98
Reconstructing data (°C)	22.09	22.53	22.27	23.93	24.01	23.81	23.68	23.36	23.36	23.05
Error	6.38%	6.51%	5.90%	1.15%	1.58%	0.97%	1.34%	2.56%	2.99%	3.89%

**Table 15.** Comparison of experimental data and reconfiguration results (reconfiguration condition 2).

Measurement Points	1	2	3	4	5	6	7	8	9	10
Experimental data (°C)	21.99	22.11	21.90	21.69	21.63	21.91	21.99	21.99	21.92	21.88
Reconstructing data (°C)	22.04	22.69	21.69	21.90	20.85	21.33	21.45	21.43	21.52	21.75
Error	0.22%	2.60%	0.94%	0.96%	3.62%	2.63%	2.44%	2.53%	1.83%	0.59%
Measurement points	11	12	13	14	15	16	17	18	19	20
Experimental data (°C)	21.72	21.87	21.96	21.86	21.92	22.26	22.32	22.30	22.38	22.31
Reconstructing data (°C)	22.06	22.40	23.49	24.30	24.47	24.10	24.05	23.37	23.72	23.80
Error	1.57%	2.40%	6.94%	11.19%	11.66%	8.27%	7.78%	4.81%	5.99%	6.70%

Figures 31 and 32 show that the average errors of reconstructed conditions 1 and 2 are 3.58% and 4.28%, respectively. Except for reconstructed condition 2 where the error of vertical surface is slightly larger, the error of each measurement point of the remaining surface is relatively small, in the range of 2%. In reconfiguration condition 2, the air velocity of air supply port 2 reaches 0.28 m/s, and that of air supply port 3 reaches 0.18 m/s, which is slightly larger than the reconfiguration condition. The large air volume leads to the uniform temperature distribution in the experiment chamber, which is the main reason for the error.

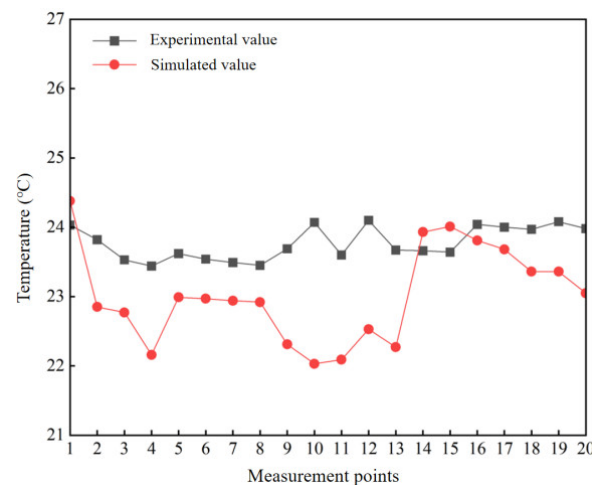


**Figure 31.** Comparison of experimental results with reconfiguration condition 1.

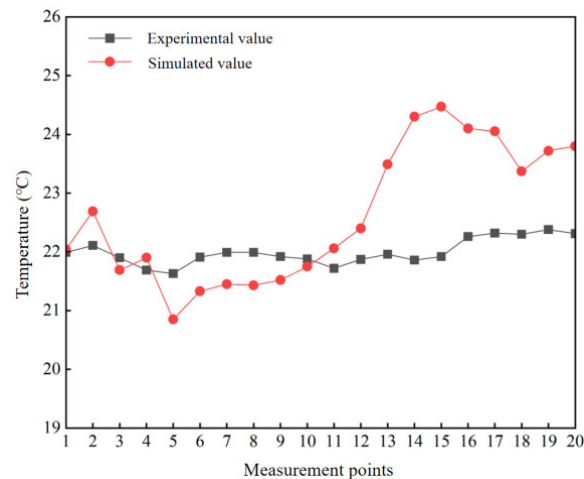


**Figure 32.** Comparison of experimental results with reconstructed data for reconfiguration condition 2.

### 5.3. Experimental Verification of the Reliability of the Search Results under the POD Method

Based on the 27 data samples obtained in Table 10, two experiments are designed in this section to verify the reliability of the POD method of finding the optimum. Firstly, three measurement points 5, 7 and 9 are selected as demand points (see Figure 24), and then, the target temperature of the demand points is set (see Table 16), and the optimal air supply parameters to meet the target temperature of the demand points are calculated by the POD search procedure (see Table 17). Next, the obtained air supply parameters are used as experimental conditions for the experiments, and the temperature values of the demand points (points 5, 7 and 9) are extracted after the internal environment of the experimental chamber has stabilised. The results are summarised in Tables 16 and 17.

**Table 16.** Target temperature at the point of demand.

Measurement Points	5	7	9
Experiment 1 Target temperature °C	23.50	24.00	24.50
Experiment 2 Target temperature °C	22.50	22.00	21.50

**Table 17.** Optimal air supply parameters calculated by the POD search procedure.

Measurement Points	1 and 2 Air Supply Speed	3 and 4 Air Supply Speed	Air Supply Temperature
Experiment 1	0.10	0.25	20.90
Experiment 2	0.24	0.10	19.40

The target temperature set in Table 1 is used to find the optimal solution within a set of 48,000 parameters using the POD search procedure, with 0.01 m/s and 0.1 °C as the unit step for speed and temperature, respectively. The optimal parameters are determined, as shown in Table 17.

The results from Table 17 are used as the air supply parameters of the environmental chamber for the experiments. After the internal environment of the environmental chamber has stabilised, the temperature values of the three target points are obtained and compared with the design target values and the error values are calculated using Equation (25). The results are shown in Tables 18 and 19. The error between the target value and the measured value for each measurement point does not exceed 2%, and the average errors for the two experiments are 1.2% and 0.8%. The measured value is very close to the target value, which proves the accuracy of the finding result based on CFD + POD method. Thus, the method can better create a non-uniform temperature field according to the demand side.

**Table 18.** Comparison of target and measured values for Experiment 1.

Measurement Point Number	5	7	9
Target value °C	23.50	24.00	24.50
Measured value °C	23.90	24.03	24.07
Error	1.7%	0.1%	1.8%

**Table 19.** Comparison of target and measured values for Experiment 2.

Measurement Point Number	5	7	9
Target value °C	22.50	22.00	21.50
Measured value °C	22.18	21.85	21.42
Error	1.4%	0.7%	0.4%

Although the error between the experimental results and the set target is relatively small, the influencing factors can still be analysed. The air supply parameters during the experiment are difficult to adjust precisely to the results obtained by the optimisation search calculation. For example, the air velocity is difficult to adjust to the exact percentile. In addition, the air velocity in both results is at the edge of the parameter interval, i.e., 0.1 m/s. Comparing the position of the measurement points and the air outlet reveals that when the air velocity is at the edge, the measurement points near the air outlet have a larger error, indicating the results are only the optimal solution within the interval.

#### 5.4. Experimental Validation of the Accuracy of Results under the Gappy POD Method

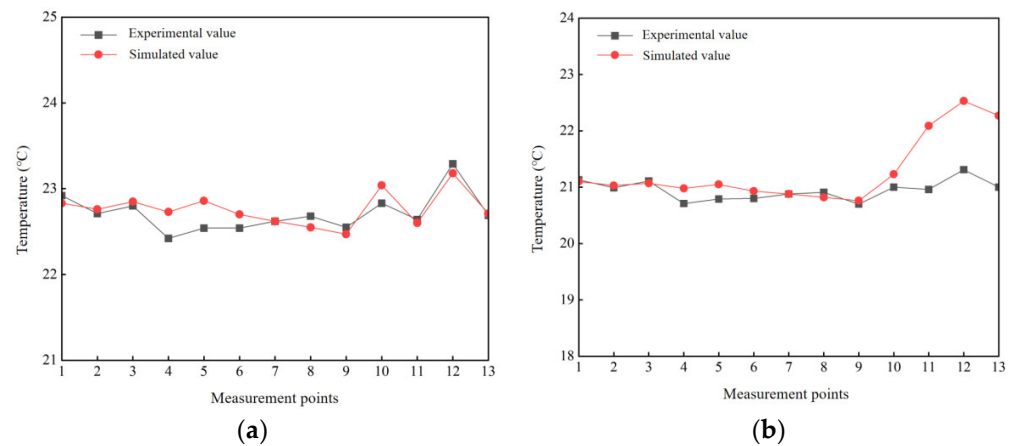
The POD method facilitates the extraction of sample data features and the establishment of a causal relationship between the air supply parameters and the indoor environmental field, thus allowing the rapid reconstruction of the flow field information for any air supply parameter. By contrast, changes in boundary conditions or environmental parameters can result in the absence of a database of samples underlying the POD method, making projecting flow field results directly using POD impossible. At this point, the gappy POD method can be used to accurately fill in the elements of the system with any missing data, with the help of a limited number of sensors combined with POD to reconstruct the flow field with a gap. Thus, the known data in this paper are the those monitored by the sensors in real time. However, both the number of sensors and the choice of position can have an impact on reconstruction accuracy. According to the summary of our existing work, the arrangement of the sensors should be centred on the emitting source in a spread-out arrangement that is more conducive to environmental creation. The sensors should be allocated to the core source area and the non-source area in order to find a balance between the number of sensors and their location.

Therefore, in this paper, measurement points 1, 2, 3, 6, 8, 9, 11, 12 and 13 in the  $z = 0.3$  m plane (see Figure 25) are designated as the sensor installation locations, and the entire flow field is reconstructed by means of nine sensors.

The working conditions set up as in Section 4.2.2 are verified experimentally, and the results of the calculations are shown in Table 20 and Figure 33. The average errors of working conditions 1 and 3 are 0.54% and 1.75%, respectively. The error of measuring points 11, 12 and 13 of working condition three in Figure 33b is higher, mainly because the air volume of air supply outlet 2 is farther than the preset value in the actual control, and the air volume control equipment is not well controlled within the preset, so it causes certain accuracy impact. To demonstrate the effect of the thirteen measurement points on the reconstructed results for the other parts not used as input, the results of the validation points are then compared individually as shown in Table 21, with an average error of 0.92% and 0.87% for the validation points in working condition 1 and working condition 3, respectively. Thus, the gappy POD combined with the finite sensor obtains a good real-time reconstructed flow field.

**Table 20.** Comparison of gappy POD calculation results and experimental results.

	Measurement Points	1	2	3	4	5	6	7
Working condition 1	Experimental data °C	22.92	22.71	22.8	22.42	22.54	22.54	22.62
	Reconstructing data °C	22.83	22.76	22.85	22.73	22.86	22.70	22.62
	Error	0.41%	0.21%	0.24%	1.36%	1.42%	0.69%	0.01%
Working condition 3	Experimental data °C	21.13	20.99	21.11	20.71	20.79	20.8	20.88
	Reconstructing data °C	21.10	21.03	21.07	20.98	21.05	20.93	20.88
	Error	0.16%	0.21%	0.21%	1.33%	1.25%	0.63%	0.02%
	<b>Measurement Points</b>	<b>8</b>	<b>9</b>	<b>10</b>	<b>11</b>	<b>12</b>	<b>13</b>	
Working condition 1	Experimental data °C	22.68	22.55	22.83	22.64	23.29	22.69	
	Reconstructing data °C	22.55	22.47	23.04	22.60	23.18	22.71	
	Error	0.59%	0.37%	0.90%	0.18%	0.49%	0.11%	
Working condition 3	Experimental data °C	20.91	20.7	21	20.96	21.31	21	
	Reconstructing data °C	20.82	20.76	21.23	22.09	22.53	22.27	
	Error	0.44%	0.27%	1.08%	5.39%	5.73%	6.05%	

**Figure 33.** Comparison of experimental results with calculated results. (a) Working condition 1 (b) Working condition 3.**Table 21.** Comparison of calculated and experimental results for validation measurement points.

Measurement Points/Working Conditions	Working Condition 1			Working Condition 3		
	Experimental Value °C	Calculated Value °C	Relative Error	Experimental Value °C	Calculated Value °C	Relative Error
4	22.42	22.73	1.36%	20.71	20.94	1.12%
5	22.54	22.86	1.42%	20.79	21.05	1.25%
7	22.62	22.62	0.01%	20.88	20.88	0.02%
10	22.83	23.04	0.90%	21.00	21.23	1.08%

## 6. Conclusions

This paper verifies the feasibility of the CFD + POD method for creating a non-uniform temperature field by building an artificial environment chamber. The accuracy of the POD method reconstruction is verified by comparing the deviation of the measured temperature values from the temperature values of the corresponding points on the reconstruction surface. Finally, the optimum air supply parameter is calculated with the target temperature of the four demand points, and experiments are carried out under this parameter to obtain the measured values of the demand points to verify the accuracy of the POD method based on the inverse solution of the demand point air supply parameter. The measured temperature values are compared with the target temperature values for analysis. A gappy POD method incorporating a small number of sensors is proposed to fill in the missing temperature field data, assuming sudden changes in the heat source or unknown environmental boundary variables. The following results are obtained:

- (1) The accuracy of the CFD simulation results is verified. Comparing the four experimental results with the simulation results reveals that the average errors between the measured and simulated temperature values are 2.15%, 3.42%, 2.79% and 1.33%, none of which exceed 4%. Thus, the simulation results can accurately reflect the distribution of the temperature field.
- (2) The accuracy of the POD method reconstruction is confirmed. Comparing the reconstructed results with the experimental results twice finds that the average errors of the reconstructed data and the experimental data are 3.58% and 4.28%, respectively. Hence, the reconstructed results are accurate and can meet the requirements.
- (3) The accuracy of the POD-based method is proven. The air supply parameters obtained by the POD method are used as the experimental conditions, and the measured temperature values at the target point are compared with the set target. The experiments are conducted twice, and the average errors between the measured temperature and the set demand temperature are 1.2% and 0.8%. Therefore, the air supply parameters obtained by the POD method are accurate and can meet the demand temperature requirements.
- (4) The accuracy of the gappy POD method reconstruction is tested when the boundary variables could not be obtained accurately. Using  $z = 0.3$  m as the reconstructed object, the gappy POD calculation results are then compared with the measured values to obtain an average error of 0.54% and 1.75% for the two sets of working conditions. This outcome demonstrates the feasibility and practicality of gappy POD combined with finite sensors for constructing the flow field in real time.

**Author Contributions:** All authors contributed to the study conception and design. Material preparation, data collection and analysis were performed by X.W., Z.C. and D.L. The first draft of the manuscript was written by Y.L. and J.Z. and all authors commented on previous versions of the manuscript. All authors have read and agreed to the published version of the manuscript.

**Funding:** This work was supported by Machinery Industry Innovation Platform Construction Project [grant number 2019SA-10-07]; Shandong Construction Department Research and Development Project [grant number K2019370]; and sponsored by Shanghai Sailing Program [grant number 20YF1432000].

**Data Availability Statement:** All data generated or analysed during this study are included in this published article.

**Conflicts of Interest:** The authors declare that they have no known competing financial interest or personal relationships that could have appeared to influence the work reported in this paper.

## References

1. Hua, P.M.; Zhao, T.Y.; Dai, W.H.; Zhang, J.L. Online control method for outdoor air rate variable setting value of VAV system based on static pressure difference control of outdoor air dampers. *HVAC* **2019**, *49*, 43–49. (In Chinese)
2. Zhao, F.; Chen, P.; Zhang, D. Multi-indicators assessment of air environment in displacement and mixing ventilation numerical method. *Eng. J. Wuhan Univ.* **2018**, *51*, 823–830.
3. Tian, L.; Lin, Z.; Liu, J.; Yao, T.; Wang, Q. The impact of temperature on mean local air age and thermal comfort in a stratum ventilated office. *Build. Environ.* **2011**, *46*, 501–510. [[CrossRef](#)]
4. Chen, F. Exploring the application of permeable design in architectural design. *Build. Mater. Decor.* **2020**, *605*, 85–86. (In Chinese)
5. Zhang, J. An early design-oriented approach to building energy optimization. *Homeownership* **2016**, *5*, 37–38. (In Chinese)
6. Tong, Z.; Liu, H.; Tong, S.; Xu, J. Inverse Design for Thermal Environment and Energy Consumption of Vehicular Cabins with PSO–CFD Method. In *Man–Machine–Environment System Engineering*; Springer: Berlin/Heidelberg, Germany, 2020.
7. Wan, X.H. Reflections on innovation in interior design—The inspiration of “lawlessness in law”. *Inter. Des.* **2004**, *4*, 11–14. (In Chinese)
8. Zhao, X.; Liu, W.; Liu, S.; Zou, Y.; Chen, Q. Inverse design of an indoor environment using a CFD-based adjoint method with the adaptive step size for adjusting the design parameters. *Numer. Heat Transf.* **2017**, *71*, 707–720. [[CrossRef](#)]
9. Zhang, T.; You, X. Inverse design of aircraft cabin environment by coupling artificial neural network and genetic algorithm. *HVAC Res.* **2014**, *20*, 836–843. [[CrossRef](#)]
10. Burrough, P.A.; McDonnell, R.; McDonnell, R.A.; Lloyd, C.D. *Principles of Geographical Information Systems*; Oxford University Press: Oxford, UK, 2015.

11. Huang, Y.; Shen, X.; Li, J.; Li, B.; Duan, R.; Lin, C.H.; Chen, Q. A method to optimize sampling locations for measuring indoor air distributions. *Atmos. Environ.* **2015**, *102*, 355–365. [[CrossRef](#)]
12. Li, J.; Li, H.; Ma, Y.; Wang, Y.; Abokifa, A.A.; Lu, C.; Biswas, P. Spatiotemporal distribution of indoor particulate matter concentration with a low-cost sensor network. *Build. Environ.* **2018**, *127*, 138–147. [[CrossRef](#)]
13. Cheng, K.-C.; Tseng, C.-H.; Hildemann, L.M. Using Indoor Positioning and Mobile Sensing for Spatial Exposure and Environmental Characterizations: Pilot Demonstration of PM<sub>2.5</sub> Mapping. *Environ. Sci. Technol. Lett.* **2019**, *6*, 153–158. [[CrossRef](#)]
14. Chen, Q. Ventilation performance prediction for buildings: A method overview and recent applications. *Build. Environ.* **2009**, *44*, 848–858. [[CrossRef](#)]
15. Liu, W.; Jin, M.; Chen, C.; You, R.; Chen, Q. Implementation of a fast fluid dynamics model in OpenFOAM for simulating indoor airflow. *Numer. Heat Transf.* **2016**, *69*, 748–762. [[CrossRef](#)]
16. Song, Z.; Murray, B.T.; Sammakia, B. A dynamic compact thermal model for data center analysis and control using the zonal method and artificial neural networks. *Appl. Therm. Eng.* **2014**, *62*, 48–57. [[CrossRef](#)]
17. Megri, C.A.; Haghghat, F. Zonal modeling for simulating indoor environment of buildings: Review, recent developments, and applications. *HVACR Res.* **2007**, *13*, 887–905. [[CrossRef](#)]
18. Song, Z.; Murray, B.T.; Sammakia, B. Airflow and temperature distribution optimization in data centers using artificial neural networks. *Int. J. Heat Mass Transf.* **2013**, *64*, 80–90. [[CrossRef](#)]
19. Cao, S.-J.; Ren, C. Ventilation control strategy using low-dimensional linear ventilation models and artificial neural network. *Build. Environ.* **2018**, *144*, 316–333. [[CrossRef](#)]
20. Zhou, L.; Haghghat, F. Optimization of ventilation system design and operation in office environment, Part I: Methodology. *Build. Environ.* **2009**, *44*, 651–656. [[CrossRef](#)]
21. Zhou, L.; Haghghat, F. Optimization of ventilation systems in office environment, Part II: Results and discussions. *Build. Environ.* **2009**, *44*, 657–665. [[CrossRef](#)]
22. Hotelling, H. Analysis of a complex of statistical variables into principal components. *J. Educ. Psychol.* **1933**, *24*, 498–520. [[CrossRef](#)]
23. Bakewell, H.P.; Lumley, J.L. Viscous Sublayer and Adjacent Wall Region in Turbulent Pipe Flow. *Phys. Fluids* **1967**, *10*, 1880–1889. [[CrossRef](#)]
24. Sirovich, L.; Kirby, M. Low-Dimensional Procedure for the Characterization of Human Faces. *J. Opt. Soc. Am. A* **1987**, *4*, 519–524. [[CrossRef](#)] [[PubMed](#)]
25. Holmes, P.; Lumley, J.L.; Berkooz, G. *Turbulence, Coherent Structures, Dynamical Systems and Symmetry*, 2nd ed.; Cambridge University Press: Cambridge, UK, 2012; pp. 68–105.
26. Li, K.; Xue, W.; Xu, C.; Su, H. Optimization of ventilation system operation in office environment using POD model reduction and genetic algorithm. *Energy Build.* **2013**, *67*, 34–43. [[CrossRef](#)]
27. Li, K.; Su, H.; Chu, J. A CFD-based test method for control of indoor environment in air-conditioned rooms. In Proceedings of the 31st Chinese Control Conference, Hefei, China, 25–27 July 2012; IEEE: Piscataway, NJ, USA, 2012; pp. 6933–6937.
28. Ghosh, R.; Joshi, Y. Rapid Temperature Predictions in Data Centers using Multi-Parameter Proper Orthogonal Decomposition. *Numer. Heat Transf.* **2014**, *66*, 41–63. [[CrossRef](#)]
29. Sha, Z.D. Low-Dimensional Modeling and Fast Optimization of Greenhouse Environment Based on Eigenorthogonal Decomposition Technique. Master's Thesis, Jiangsu University, Zhenjiang, China, 2020. (In Chinese).
30. Elhadidi, B.; Khalifa, H.E. Application of Proper Orthogonal Decomposition to Indoor Airflows. *Ashrae Trans.* **2005**, *111*, 625–634.
31. Everson, R.; Sirovich, L. Karhunen–Loève procedure for gappy data. *J. Opt. Soc. Am. A* **1995**, *12*, 1657–1664. [[CrossRef](#)]
32. Lei, J.; Liu, S. Temperature field reconstruction of partial measurement data based on gappy orthogonal decomposition. *IET Sci. Test Technol.* **2013**, *7*, 171–179. (In Chinese)
33. Sun, S.X. Research on Wind Field Reconstruction Based on Computational Fluid Dynamics and Optimized Data Sources. Ph.D. Thesis, North China Electric Power University, Beijing, China, 2020. (In Chinese).
34. Tsering-xiao, B.; Xu, Q. Gappy POD-based reconstruction of the temperature field in Tibet. *Theor. Appl. Climatol.* **2019**, *138*, 1179–1188. [[CrossRef](#)]
35. Willcox, K. Unsteady flow sensing and estimation via the Gappy proper orthogonal decomposition. *Comput. Fluids* **2006**, *35*, 208–226. [[CrossRef](#)]
36. Li, J. Research and Application of Aerodynamic Shape Design Method for High Performance Aircraft. Ph.D. Thesis, Northwestern Polytechnic University, Fremont, CA, USA, 2014. (In Chinese)
37. Mifsud, M.; Vendl, A.; Hansen, L.U.; Görtz, S. Fusing wind-tunnel measurements and CFD data using constrained Gappy proper orthogonal decomposition. *Aerosp. Sci. Technol.* **2019**, *86*, 312–326. [[CrossRef](#)]
38. Xing, X.; Dao, M.H.; Zhang, B.; Lou, J.; Tan, W.S.; Cui, Y.; Khoo, B.C. Fusing sensor data with CFD results using Gappy POD—ScienceDirect. *Ocean. Eng.* **2022**, *246*, 110549. [[CrossRef](#)]
39. Wang, X.; Zhao, J.; Wang, F.; Song, B.; Zhang, Q. Air supply parameter optimization of a custom nonuniform temperature field based on the POD method. *Build. Environ.* **2021**, *206*, 108328. [[CrossRef](#)]
40. Luo, Y. Temperature Field Reconstruction of ultra-Supercritical CFBB Based on CFD and Reduced-Order Methods. Ph.D. Thesis, Guizhou University, Guiyang, China, 2022. (In Chinese)

41. Chen, X.B. Analysis of the Internal Flow Field of Centrifugal Pumps Based on Characteristic Decomposition and Its Performance Optimization Research. Ph.D. Thesis, Lanzhou University of Technology, Lanzhou, China, 2022. (In Chinese)
42. Yu, B.; Tong, Y.; Hu, P.; Gao, Q. A novel inversion approach for identifying the shape of cavity by combining Gappy POD with direct inversion scheme. *Int. J. Heat Mass Transf.* **2020**, *150*, 119365. [[CrossRef](#)]

**Disclaimer/Publisher's Note:** The statements, opinions and data contained in all publications are solely those of the individual author(s) and contributor(s) and not of MDPI and/or the editor(s). MDPI and/or the editor(s) disclaim responsibility for any injury to people or property resulting from any ideas, methods, instructions or products referred to in the content.